Visible to near infrared highly sensitive microbiosensor based on surface plasmon polariton with external sensing approach

M.S. Aruna Gandhi[a], K. Senthilnathan[b], P. Ramesh Babu[b], Qian Li[a,*]

[a] *School of Electronics and Computer Engineering, Peking University, Shenzhen 518055, China*
[b] *School of Advanced Sciences, Vellore Institute of Technology, Vellore 632014, India*

ARTICLE INFO

ABSTRACT

We propose a simple geometric, highly responsive and miniaturized surface plasmon polariton microbiosensor using a photonic quasicrystal fiber. Here, we consider gold as plasmonic material as the external coating for exciting the surface plasmon to detect the refractive index of the external analyte sensing to facilitate the practical realization. Further, we carry out detailed characteristics evaluations such as wavelength and amplitude sensitivities, resolution, full-width at half maximum, the figure of merit, signal to noise ratio and detection limit for both 6-fold and 8-fold plasmonic sensors. The proposed 6 and 8-fold sensors show a maximum sensitivity of 28,000 nm/RIU for an analyte range of 1.41–1.42 and 27,000 nm/RIU for an analyte range of 1.4–1.41, respectively. While the figure-of-merit of the 6-fold sensor is 491, for the 8-fold sensor, it is 231. Besides, the structural parameters and the arrangements of the air-holes in cladding region add to the sensing performance. The proposed sensing systems operate for a wide range of wavelengths from 600 to 1300 nm. Thus, the proposed sensors might turn out to be promising candidates for the refractive index-based biological and chemical detections.

Introduction

In recent times, there has been a considerable interest for the realization of simple, light-weight, low-cost and rapidly detecting photonic devices for catering to the needs of clinical diagnosis [1], health care [2] and environmental monitoring [3]. In this direction, several current advances in plasmonic sensor-based fiber optic probes for biological applications have been reported [4]. Of late, the surface plasmonic resonance (SPR) sensors are the most widely investigated type for their enhanced sensing performances and point-of-care applications [5–7]. For the first time, SPR prism coupling-based sensing technique was introduced by Liedberg et al. in 1983 for the applications of biological and chemical sensing [8]. In general, the prism coupled with plasmonic material is deployed in SPR-based sensors. For the applied incident light, the free electrons of the metal surface oscillate and generate the surface plasmonic wave in the interface of metal and dielectric [9,10]. The prism-based plasmonic sensors are largely utilized for the advantages of an aperture and their suitability for remote sensing applications. On the downside, they face a limitation owing to their bulky size [11]. Very recently, compact sensors having been realized using a specialty fiber called photonic crystal fiber (PCF) [12,13]. The PCF-based plasmonic sensor works on the basis of the evanescent wave which is generated by the surface plasmonic wave that propagates

between the metal-dielectric interface point [14]. At a particular input wavelength, the phase matching point occurs when the real effective refractive index of the fundamental mode and that of the surface plasmonic mode match such that the confinement loss of imaginary effective index mode turns maximum, that, in turn, helps analyze various biological and chemical samples. [15]. A new class of fibers called photonic quasicrystal fiber (PQF), with an aperiodic arrangement of air-holes in the cladding region, exhibits unique optical waveguide properties such as birefringence, low dispersion and high confinement loss [16,17]. For the first time, SPR based PQF refractive index (RI) biosensor has been numerically investigated for studying the sensing properties [18]. Recently, the liquid refractive index sensor based on a 2D 10-fold photonic quasicrystal has been reported [19]. Of late, an octagonal Penrose-type PQF with dual-cladding has been proposed that has effectively improved its optical properties [20]. A new phenomenon of "loss spikes" has been reported in a 6-fold symmetric double cladding PQF with the influence of inner and outer air-filling fraction on effective area [21]. A novel U-shaped external PQF sensor based on SPR have been proposed for RI sensing which provides new design idea for the RI sensor with high sensing performances [22]. A 6-fold PQF with a trapezoidal analyte channel based SPR sensor for analyzing different liquid analyte refractive indices has also been reported [23]. However, using better plasmonic materials, a low-cost sensing SPR based RI
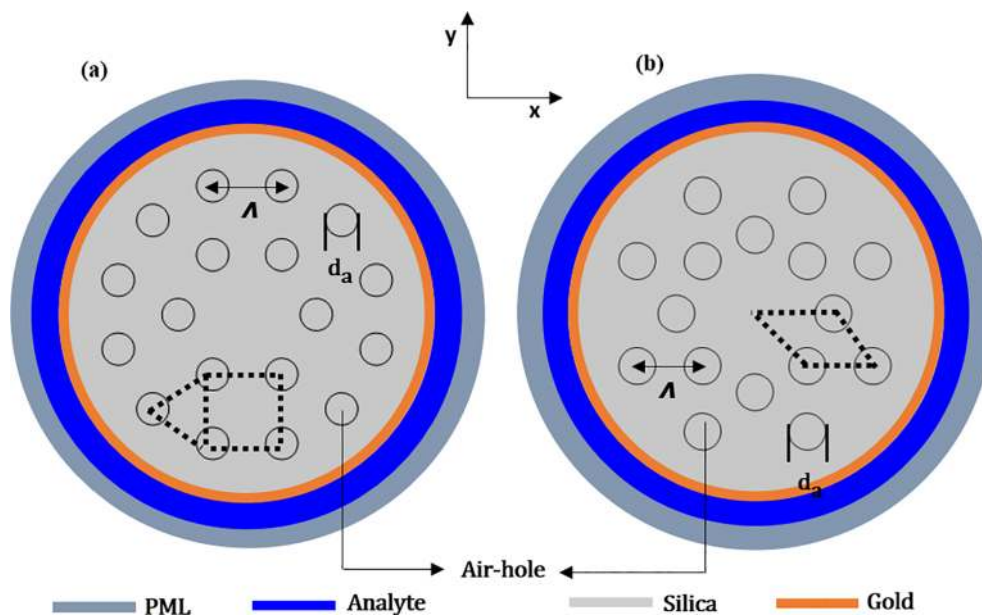

Fig. 1. The geometrical cross-section of the proposed PQF-RIBS (a) 6-fold and (b) 8-fold quasicrystal tilling.

sensors are currently being aimed at. From literature, we understand that gold and silver are widely used as plasmonic materials, of which, silver provides relatively sharper SPR peaks but easily gets oxidized [24]. In contrast, gold supports large resonance peak shift and also maintains the chemical stability for the liquid samples over other novel materials [4,25].

To date, numerous SPR-based microstructured optical sensors have been reported and classed according to their internal sensing and external sensing approaches. Internal sensing limits fabrication feasibility as it needs selective filling and also liquid infiltrations are highly challenging [4]. However, external sensing method provides a promising experimental realization. Furthermore, the D-shaped PCF based SPR sensor provides better sensing performances over other external sensing techniques [26]. D-shaped fiber structure also needs precise coating care to overcome the surface roughness which may obstruct the performance of the sensor. Additionally, a new idea of introducing the analyte medium on the surface of the externally coated metal layer on the cladding of the fiber has been proposed [9,10,26,27]. An analyte under investigation (AUI) with external sensing channel turns simple and efficient by pouring and dripping the analyte upon the plasmonic layer. The following research works lean upon the external sensing approach for enhancing the sensing performances. Recently, Haider et al. reported a highly sensitive PCF based plasmonic sensor exhibiting a maximum amplitude sensitivity of 2843 RIU^{-1} with a sensor resolution of 3.5×10^{-6} RIU in the RI range of 1.33–1.41 [28]. Hasan et al. demonstrated an SPR biosensor-based on dual-polarized spiral PCF that exhibits a maximum sensitivity of 4600 and 4300 nm/RIU in x- and y-polarized modes, respectively, for an analyte with a RI of 1.37 [29]. Same research group has proposed a highly sensitive self-calibration biosensor based on SPR-PCF that exhibits a high RI sensitivity of 10,000 nm/RIU with the quasi-TE mode [30]. Chakma et al. proposed a particularly sensitive circular lattice PCF based SPR sensor capable of providing a maximum sensitivity of 9000 nm/RIU with the analyte of RI ranging from 1.34 to 1.37 [31]. Xudong et al. proposed a gold-plated PCF refractive index SPR based sensor that shows a maximum sensitivity of 11,000 nm/RIU and a maximum amplitude sensitivity of 641 RIU^{-1} [32]. Zhou et al. have proposed a practical sensor based on SPR in a ring-shaped core PCF that displays a maximum wavelength and amplitude sensitivity of 6900 nm/RIU and 132 RIU^{-1} in the analyte RI range from 1.33 to 1.41 [33]. Rifat et al. investigated a simple PCF structured biosensor by coating the chemically stable gold on the

outer surface for realizing the external sensing approach, thereby achieving the wavelength and amplitude sensitivity of 4000 nm/RIU and 478 RIU^{-1}, respectively, in the sensing range of 1.33–1.37 [34]. Consequently, coating the metal on the PCF surface externally turns out to be the best sensing approach. In our previous work, we have numerically investigated a simple structured external sensing PCF-RIBS exhibiting a highest spectral sensitivity of 12,000 nm/RIU and amplitude sensitivity of 11,412 RIU^{-1} in the RI sensing environment from 1.44 to 1.45 [35].

In this line, to enhance the device performances of the external sensing plasmonic sensors with gold as a coating material, we model two different folds of air-holes such as 6 and 8-fold photonic quasicrystal fiber based refractive index biosensors (PQF-RIBS) using finite element method. The sensing performances such as spectral and amplitude sensitivities are analyzed by using wavelength and amplitude interrogation technique which can operate in a wide wavelength spectrum from visible to near IR region. Further, we also investigate the properties, namely, signal-to-noise ratio, detection limit, sensor resolution and figure of merits. We use the chemically stable gold as a plasmonic material which is very much adaptable to experimental fabrication for external sensing approach. The proposed 6 and 8-fold PQF-RIBS sensors are compact, simple and efficient in the detection of unknown AUI by dripping or flowing on the external gold surface.

Design and analysis

We have reported a novel 6 and 8-fold photonic quasicrystal fiber based Micro biosensors by using finite element method. Geometrical cross-sections of 6 and 8-fold PQF-RIBS are shown in Fig. 1(a) and (b), respectively. The air-hole arrangements in the cladding region conform to the practice relating to the angular distribution from the center of the PQF-RIBS by a scattering radius $r_s = \Lambda \times \sin(\pi/n)$, where *n* is the number of folds and Λ is the pitch or lattice constant. The term 'fold' is a measure of rotational symmetry in the proposed PQF-RIBS, where we design the air-holes with the repetitions of the square and equilateral triangles and the same is shown in Fig. 1(a). The 8-fold PQF-RIBS constitutes the repetition of air-holes in the form of rhombus structure as shown in Fig. 1(b). The diameter, d_a, of the air-hole is 1 μm, the thickness of the gold layers is 30 nm and pitch, Λ, as 3 μm in both the geometries of the proposed PQF-RIBS. The circular perfectly matched layer (PML) and scattering boundary conditions are used to avoid the

reflection of light and analyze the propagation loss by confining light in the microstructured optical fiber [14]. To improve the accuracy of the results, the proposed PQF-RIBSs are simulated with the effective PML for the convergence analysis by revising the mesh size and PML thickness.

The RI of fused silica was obtained using the Sellmeier Equation as follows [36],

$$n^2(\lambda) = 1 + \frac{B_1\lambda^2}{\lambda^2 - C_1} + \frac{B_2\lambda^2}{\lambda^2 - C_2} + \frac{B_3\lambda^2}{\lambda^2 - C_3},$$ (1)

where n is the wavelength-dependent RI of fused silica and λ is the operating wavelength in μm. B_1, B_2, B_3, C_1, C_2 and C_3 are Sellmeier constants and they are 0.69616300, 0.407942600, 0.897479400, $0.00467914826 \times 10^{-3}\,\mu m^2$, $0.0135120631 \times 10^{-2}\,\mu m^2$ and $97.9340025\,\mu m^2$, respectively. The plasmonic metal layer with the thickness from 20 to 50 nm has been analyzed by coating on the external surface of the proposed PQF-RIBS. The dielectric constant of the gold can be obtained from the Drude-Lorentz model as follows [37],

$$\epsilon_{Au} = \epsilon_{\infty} - \frac{\omega_D^2}{\omega(\omega + j\gamma_D)} - \frac{\Delta \epsilon \, \Omega_L^2}{(\omega^2 - \Omega_L^2) + j\Gamma_L^{\omega}},$$ (2)

where ϵ_{Au} is the permittivity of gold, ϵ_{∞} is the permittivity at a higher frequency with the value of 5.9673, ω is an angular frequency, as $\omega = 2\pi c/\lambda$, where c is the velocity of light in vacuum. Here, $\omega_D/2\pi = 2113.6$ THz, where ω_D is the plasma frequency, $\gamma_D/2\pi = 15.92$ THz, where γ_D is the damping frequency and $\Delta \epsilon = 1.09$ is weighting factor. The oscillator strength and spectral width of the Lorentz oscillators are calculated as $\Omega_L/2\pi = 650.07$ THz and $\Gamma_L/2\pi = 104.86$ THz, respectively.

Results and discussion

In this section, we discuss the sensing performances of the proposed PQF-RIBS, namely, phase matching condition, confinement loss, wavelength sensitivity, amplitude sensitivity, resolution, figure-of-merit, full-width at half-maximum, signal-to-noise ratio and detection limit. First, we calculate the real and imaginary parts of the effective refractive index (n_{eff}) of the core-guided mode and surface plasmon polariton (SPP) mode as a function of wavelength.

Fig. 2(a)–(d) explain the electric field modal distribution of the 6 and 8-fold PQF-RIBS. It is obvious that the strong mode field coupling between the core-guided mode and SPP mode appears for 8-fold PQF-RIBS. With the increase in the number of air-holes, the n_{eff} contrast between the core-guided mode and SPP mode reduces and results in strong coupling field. The confinement loss is calculated with the imaginary part of n_{eff} values of the core-guided mode field by using the following relation,

$$\alpha_{loss}\left[\frac{dB}{cm}\right] = 8.686 \times \frac{2\pi}{\lambda} \cdot Im[n_{eff}] \times 10^4,$$ (3)

where λ represents the operating wavelength, and $Im[n_{eff}]$ is the imaginary part of n_{eff} of the core-guided fundamental mode. Next, we calculate the dispersion relation of the core-guided mode and SPP mode. The numerical investigation of the proposed PQF-RIBS for the microfluidic environment sensing explains that the real part of the core-guided mode field exactly intersects with the real part of surface plasmon polariton mode field where the confinement loss of core-guided mode also turns maximum as depicted in Fig.2(e). The so-called phase matching condition is achieved at 0.66 μm and 0.76 μm for 6 and 8-fold PQF-RIBS, respectively. The n_{eff} values get reduced and confinement loss values are increased, when the arrangement of air-holes becomes circular in the 8-fold PQF-RIBS when compared to the 6-fold PQF-RIBS. It also shows the generation of strong mode field coupling for the 8-fold PQF-RIBS. From literature, the major facilities of an ultra-low loss microstructured biosensor have an extremely sensitive

performance, label-free, capabilities of multi analytes detection, which can be used in medical diagnosis, environmental safety, drug detection [29].

Next, we extend our investigation by varying the RI of the analyte for 6-fold and 8-fold PQF-RIBS. Fig. 3(a) provides the confinement loss analysis for 6-fold PQF-RIBS when the RI of the analyte refractive index environment of 1.31–1.42 for the wavelength range from 0.5 to 1.3 μm. Fig. 3(b) shows that the confinement loss is much pronounced for the analyte-RI environment of 1.31–1.41 for 8-fold in comparison with the 6-fold PQF-RIBS. For each analyte-RI value of both 6 and 8-fold PQF-RIBS, the resonance peak wavelength is listed in Table 1. From Fig. 3(a) and (b), it is obvious that the propagation loss increases and also gets shifted towards longer wavelength with the increase in RI of the analyte. We note that the propagation loss is very less in the visible region when compared to the near IR region. It is due to the RI-contrast between the core-guided mode and SPP mode that gets reduced and eventually, results in the strong coupling. When the propagation field generates the high evanescent field and excites more surface-electrons, the loss becomes saturated near the longer wavelength region as shown in Fig. 3(a) and (b) for analyte-RI of 1.42 and 1.41, respectively. Thus, the proposed sensing systems operate in the wide range of wavelength from visible to near infrared region.

Next, we compute the wavelength sensitivity of a SPR sensor based on the wavelength interrogation method and the same is defined as

$$S_{\lambda}[nm/RIU] = \frac{\Delta\lambda_{peak}}{\Delta n_a},$$ (4)

where $\Delta\lambda_{peak}$ is the shift of peak position and Δn_a is the change of the analyte-RI. In Fig. 3(a), the minimum core-guided modal loss is 0.18 dB/cm at $n_a = 1.31$ and the maximum loss is 10 dB/cm at $n_a = 1.42$. Fig. 3(b) shows the minimum propagation loss of 3.49 dB/cm for $n_a = 1.31$ and maximum loss of 19.5 dB/cm at $n_a = 1.41$. The maximum resonant wavelength shift is achieved from 0.91 to 1.19 μm (0.28 μm) for n_a varying from 1.41 to 1.42. It brings the maximum sensitivity of 28,000 nm/RIU for 6-fold PQF-RIBS. The 8-fold PQF-RIBS provides resonant wavelength shift from 1.02 to 1.29 μm (0.27 μm) for n_a varying from 1.40 to 1.41 and achieves a wavelength sensitivity of 27,000 nm/RIU. The resonant wavelength, peak shift and its corresponding wavelength sensitivity for each value of analyte are listed for both 6 and 8-fold PQF-RIBS in Table 1.

Further, we calculate sensor resolution as another important parameter of the PQF-RIBS that provides how good the device is in detecting a minimum variation in analyte-RI by using the equation,

$$R[RIU] = \Delta n_a \times \frac{\Delta\lambda_{min}}{\Delta\lambda_{peak}}.$$ (5)

In Eq. (5), Δn_a is the analyte-RI variation, $\Delta\lambda_{min}$ represents the instrumental peak-wavelength resolution (assumed to be 0.1 μm) and $\Delta\lambda_{peak}$ is maximum resonance wavelength peak shift. Table 1 provides detailed values of resolution for both 6 and 8-fold PQF-RIBS. The maximum resolution of the proposed 6 and 8-fold PQF-RIBS are 3.5×10^{-7} RIU and 9.8×10^{-7} RIU, respectively. The polynomial fitting of the resonant wavelength with its relevant peak loss for both 6 and 8-fold PQF-RIBS are depicted in Fig. 4(a) and (b), respectively. The proposed 6 and 8-fold PQF-RIBSs show better R^2 value of 0.98075 and 0.95849, respectively, in the analyte-RI index environment from 1.37 to 1.42 which holds good for the indication of a continuous sensing response.

Next, we calculate the amplitude sensitivity of the proposed PQF-RIBS according to the following equation,

$$S_A(\lambda)[RIU^{-1}] = -\frac{1}{\alpha(\lambda, n_a)}\frac{\partial\alpha(\lambda, n_a)}{\partial n_a}.$$ (6)

In Eq. (6), $\alpha(\lambda, n_a)$ is the initial loss and $\partial\alpha(\lambda, n_a)$ is the loss difference of two-loss spectra with its adjacent analyte-RI. From Fig. 5(a) and (b) represent variation of the amplitude sensitivity for 6 and 8-fold PQF-RIBS, respectively. The maximum amplitude sensitivity is achieved as
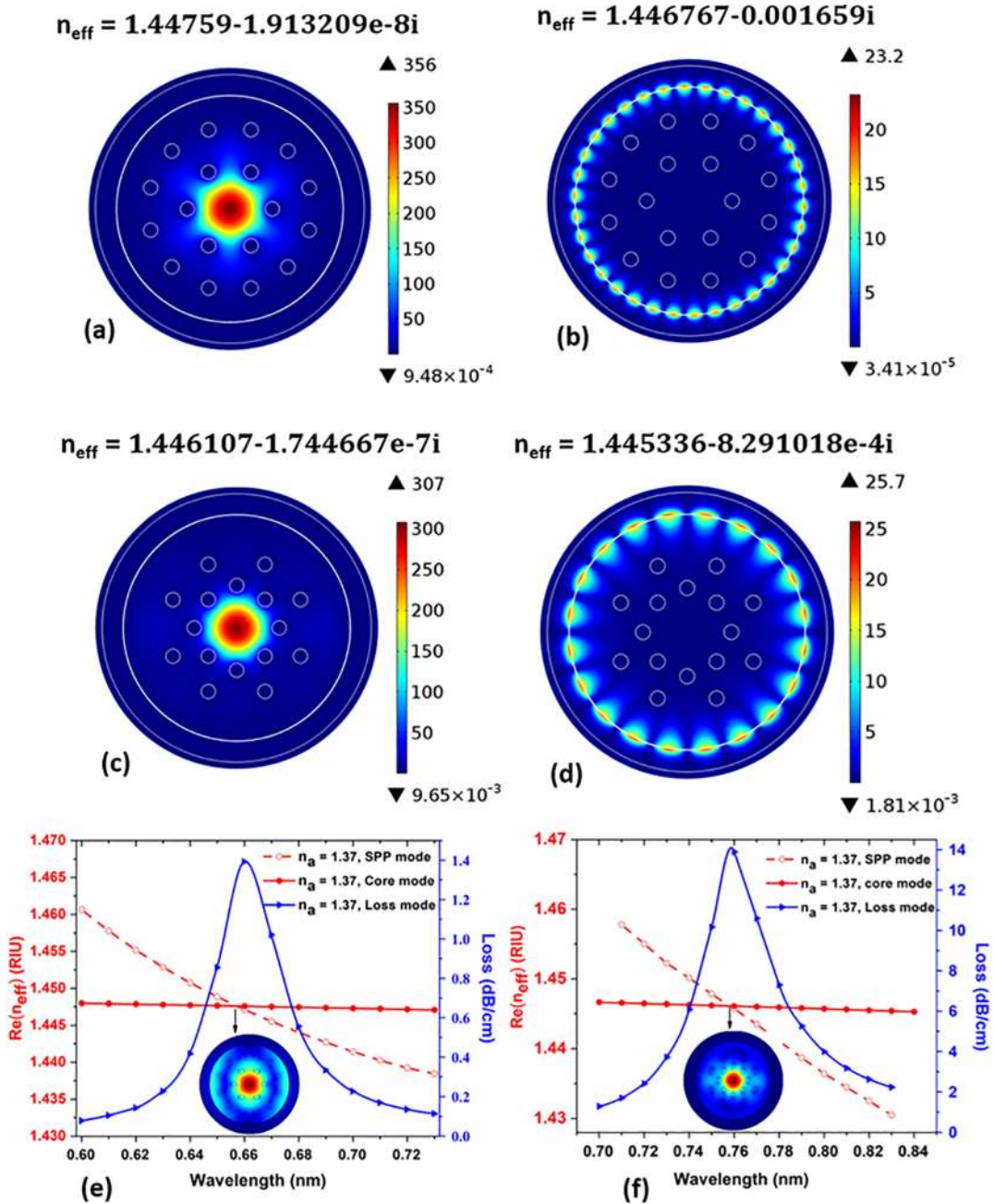
Fig. 2. (a) and (b) are the fundamental core-guided and SPP modes for 6-fold PQF-RIBS, (c) and (d) are the core-guided and SPP modes of 8-fold PQF-RIBS with the diameter, $d_a = 1\,\mu m$, $t_g = 30\,nm$ and the analyte-RI is 1.37, (e) and (f) Phase matching condition of the proposed 6 and 8-fold PQF-RIBS with the diameter, $d_a = 1\,\mu m$, $t_g = 30\,nm$ and the analyte-RI is 1.37. The inset field plots on Figs. 2(e) and (f) describes the coupling process of the proposed plasmonic sensors.

$1095\,RIU^{-1}$ and its corresponding resolution is $9.1 \times 10^{-8}\,RIU$ when the analyte-RI is 1.41 for 6-fold PQF-RIBS. The 8-fold PQF-RIBS shows the lowest and highest amplitude sensitivities of $86\,RIU^{-1}$ and $490\,RIU^{-1}$ at $n_a = 1.40$ and 1.38, respectively. The amplitude sensitivity and its corresponding resolution values for each analyte-RI are listed in Table 1 for both 6 and 8-fold PQF-RIBS. From Fig. 5(a), it is clear that, with the increase of n_a, the resonance peak value increases for 1.37 to 1.40 and decreases for $n_a = 1.41$. Eventually, the FWHM is increased for increasing analyte-RI.

In addition to the sensitivity and sensor resolution, the signal-to-noise ratio (SNR), detection limit (δn) and figure of merits (FOM) are also significant to estimate the sensor performance. These parameters can be calculated by the following relations [38]:

$$SNR = \frac{\Delta\lambda_{res}}{\Delta\lambda_{1/2}}, \tag{7}$$

$$\delta n = \frac{\Delta\lambda_{1/2}}{1.5(SNR)^{0.25}}, \tag{8}$$

$$FOM = \frac{S}{\Delta\lambda_{1/2}}, \tag{9}$$

where $\lambda_{1/2}$ is the FWHM. Here it is noted that the FWHM increases in both 6 and 8-fold PQF-RIBS with the increase of analyte-RI. Table 1 provides the sensor performances of SNR, detection limit, and FOM. When the n_a value increases, propagation loss spectrum gets broadened and as a result, the FWHM value also increases. The highest FWHM for 6 and 8-fold PQF-RIBS are 57 nm and 117 nm, respectively. This results in the maximum FOM of 491 and 231 for 6 and 8-fold PQF-RIBS,
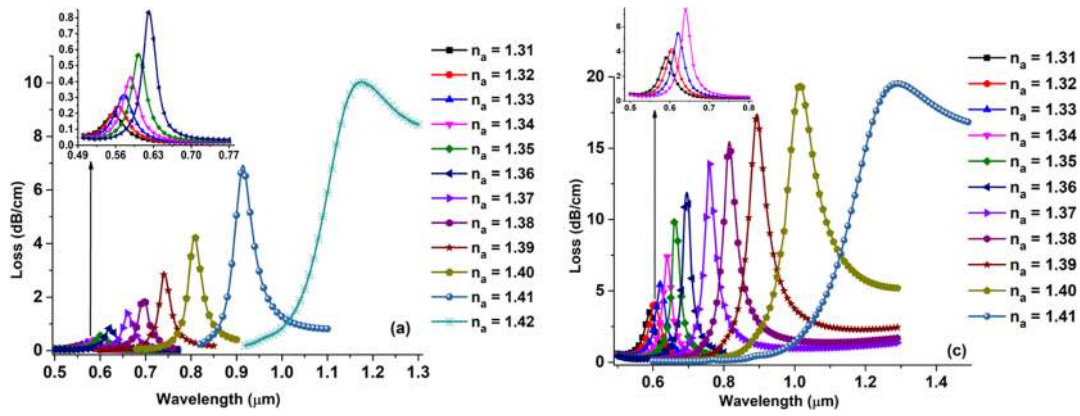
Fig. 3. Loss spectra of the core-guided mode when the analyte-RI environment is varied for (a) 6-fold and (b) 8-fold PQF-RIBS.

Table 1
Sensing performance analysis of the proposed plasmonic sensor.

| Analyte-RI	Resonance peak wavelength (nm)	Spectral sensitivity (nm/RIU)	Spectral resolution (RIU)	Amplitude sensitivity (RIU^{-1})	SNR	Detection limit	FWHM (nm)	FOM
6-Fold								
1.31	550	1000	1×10^{-4}	65	0.18	56	55	18
1.32	560	1000	1×10^{-4}	85	0.21	46	47	21
1.33	570	1000	1×10^{-4}	117	0.23	40	42	23
1.34	590	1000	1×10^{-4}	175	0.25	36	39	25
1.35	600	2000	5×10^{-5}	287	0.57	26	35	57
1.36	620	4000	2.5×10^{-5}	556	1.29	19	31	129
1.37	660	4000	2.5×10^{-6}	695	1.29	19	31	129
1.38	700	4000	2.5×10^{-6}	933	1.29	19	31	129
1.39	740	7000	1.4×10^{-6}	1408	2.25	20	38	184
1.40	810	10000	1×10^{-6}	1759	2.5	21	40	250
1.41	910	28000	3.5×10^{-7}	1095	4.91	25	57	491
1.42	1190	N/A	N/A	N/A	N/A	N/A	N/A	N/A
8-Fold								
1.31	590	1000	1×10^{-4}	98	0.23	41	43	23
1.32	600	2000	5×10^{-5}	142	0.5	31	40	50
1.33	620	2000	5×10^{-5}	217	0.52	29	38	52
1.34	640	4000	2.5×10^{-5}	360	1.25	20	32	125
1.35	660	4000	2.5×10^{-5}	512	1.37	17	29	137
1.36	700	6000	1.66×10^{-5}	1121	2.14	15	28	214
1.37	760	6000	1.3×10^{-6}	463	1.57	22	38	157
1.38	820	7000	1.21×10^{-6}	490	1.37	31	51	1.37
1.39	890	13000	1.12×10^{-6}	485	1.96	37	66	197
1.40	1020	27000	9.80×10^{-7}	275	2.30	63	117	231
1.41	1290	N/A	7.75×10^{-7}	N/A	N/A	N/A	N/A	N/A
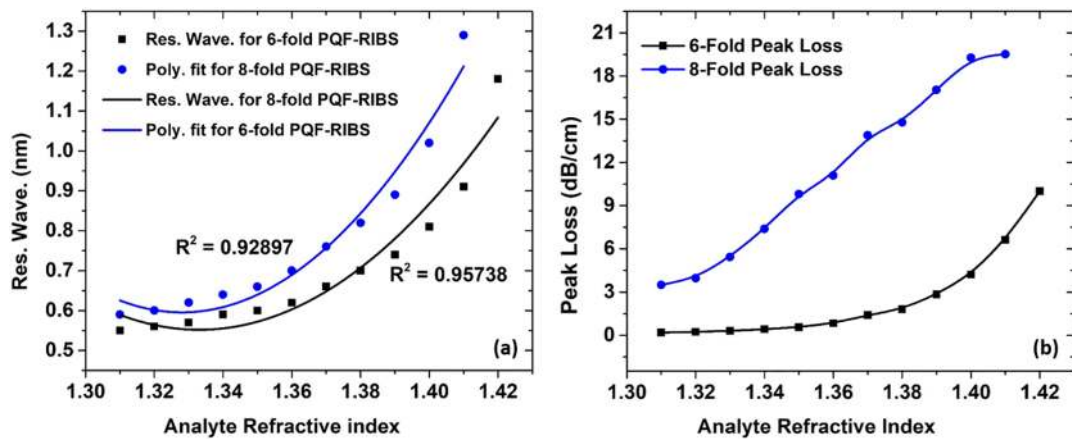
Fig. 4. (a) and (b) Resonant wavelength and peak loss as a function of analyte-RI for both 6 and 8-fold PQF-RIBS.
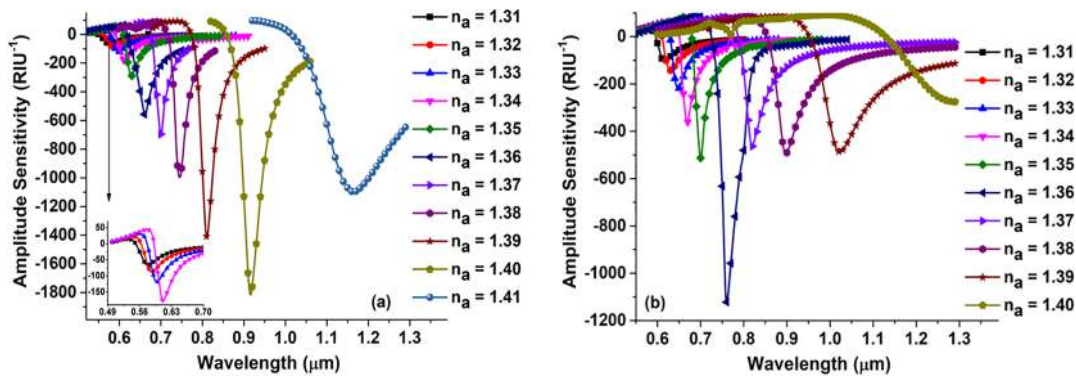
Fig. 5. Amplitude sensitivity as a function of wavelength with the various analyte-RI for (a) 6 and (b) 8-fold PQF-RIBS.
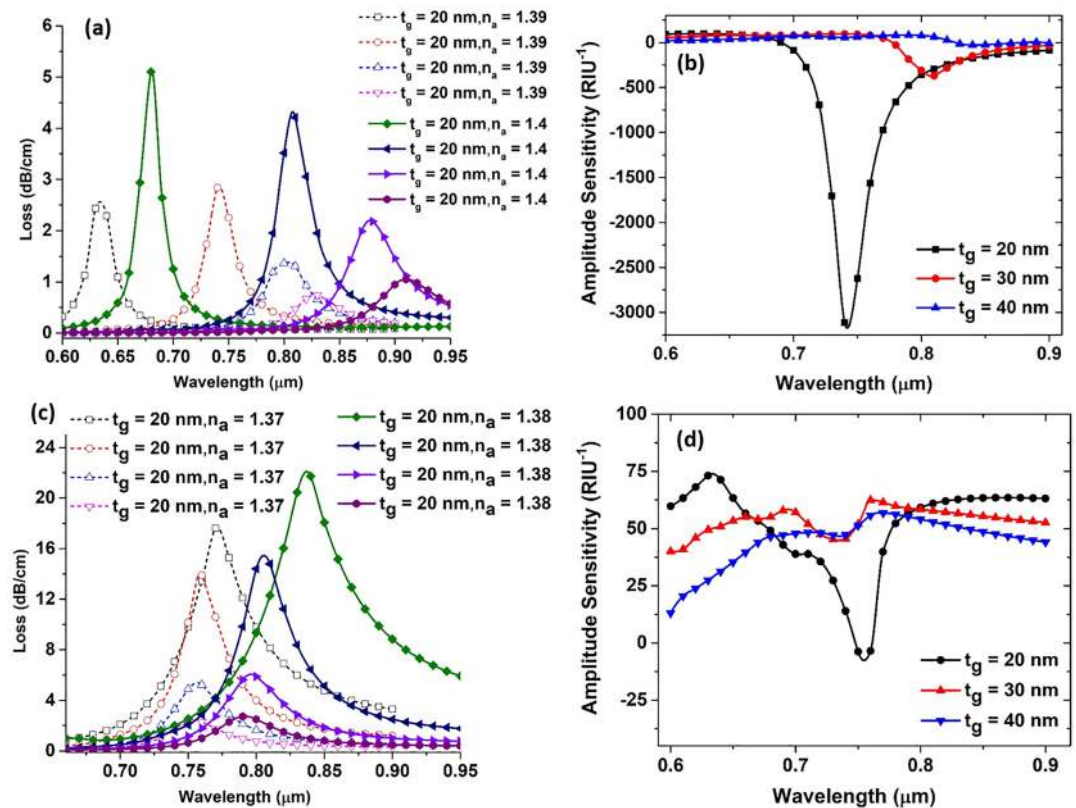

Fig. 6. (a) and (c) Loss spectra of the core guided-mode when the thickness of the metal is varied from 20 to 50 nm for 6 and 8-fold PQF-RIBS. (b) and (d) Amplitude sensitivity of various gold layer thickness for $n_a = 1.39$ and 1.37 for 6 and 8-fold PQF-RIBS.

respectively. To achieve high sensing performances, the FOM should be as maximum as possible.

Gold is used as plasmonic material to generate the SPP mode which propagates along the metal-dielectric interface. Consequently, the gold layer has a strong influence on the proposed PQF-RIBS sensing performance. Fig.6(a) shows the loss spectra variation of the gold layer thickness with analyte-RI 1.39 and 1.4 and for the diameter of air-hole is 1 μm. For the gold layer thickness of $t_g = 30$ nm, the loss value reduces to 0.7381 dB/cm. When the gold layer thickness increases, the confinement loss decreases. It demonstrates a less penetration of the electric field on the sensing layer. Fig. 6(c) shows the loss variation for 8-fold PQF-RIBS with the analyte-RI of 1.37 and 1.38, when the $d_a = 1$ μm. Fig. 6(b) and (d) show the amplitude sensitivity for $t_g = 20$, 30 and 40 nm for 6 and 8-folds. The 6-fold PQF-RIBS provides 3111, 369 and 28 RIU^{-1} for the resonant wavelengths 0.74, 0.81 and 0.84 μm, respectively. As the n_a variation is a significant impact on the propagation loss, the increase of the index contrast between core and

cladding due to the increase of n^a results in decreasing of the loss depth, hence the blue shift is observed as shown in Fig. 6(b). For 8-fold PQF-RIBS, the amplitude sensitivity decreases gradually and provides 4 RIU^{-1}, -62 RIU^{-1} and -57 RIU^{-1} when the resonant wavelength is shifted from 0.75, 0.76 and 0.77 μm. The maximum damping loss appears very high for larger gold thickness and shows better for $t_g = 30$ nm for the proposed 6-fold PQF-RIBS. However, for the 8-fold PQF-RIBS, the damping loss is high for $t_g = 20$ nm and hence, we choose $t_g = 30$ nm. Additionally, we calculate the SNR and detection limit for the proposed sensors and listed the comparison in Table 1. With the analysis of damping loss and SNR, we optimize t_g to be 30 nm for sensing performances of both 6 and 8-fold PQF-RIBS. It is also important to note that the phase-matching resonant wavelength is shifted with varying the gold layer thickness. Consequently, this proves that the proposed sensors are potential to sense the nanoparticle-interaction on the plasmonic surface.
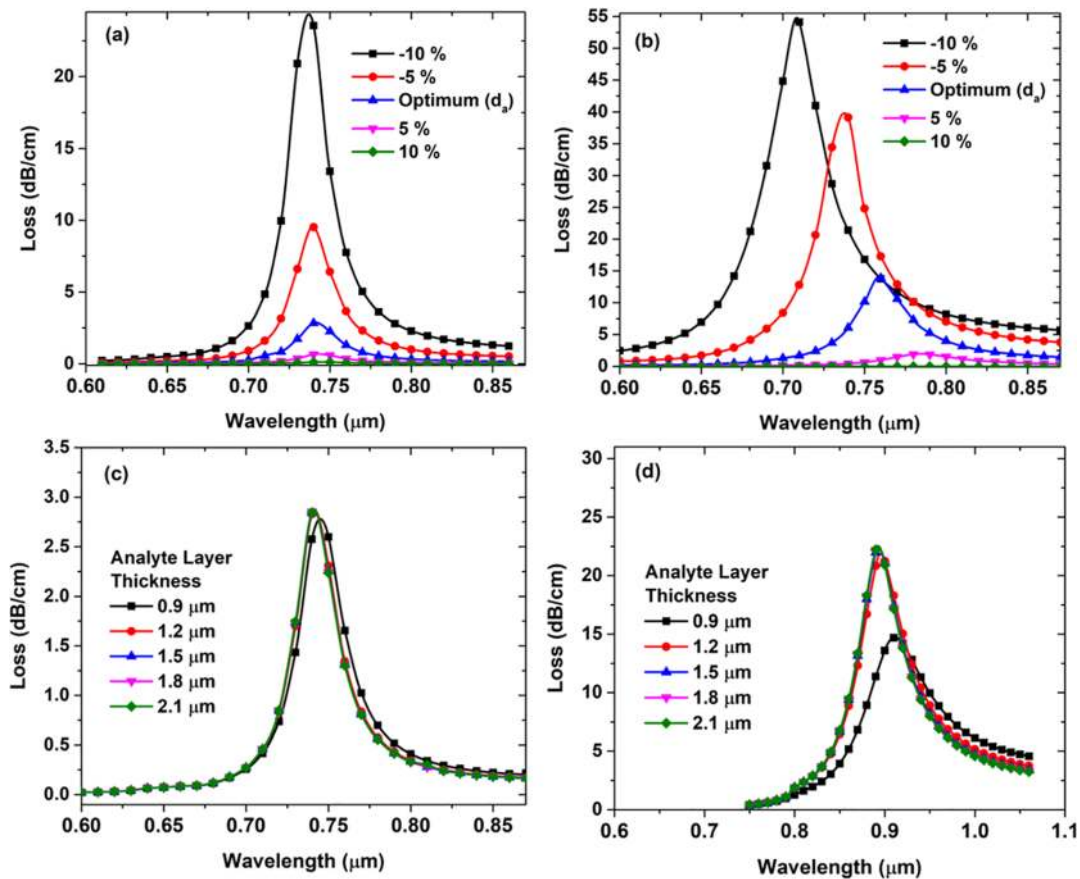
Fig. 7. (a) and (b) Scaled-down-air-hole diameter d_a effects on sensing performance for 6 and 8-fold PQF-RIBS. (c) and (d) Liquid layer thickness effects on sensing performance for 6 and 8-fold PQF-RIBS.

Fabrication tolerance investigation

From experimental approach, by maintaining the phase-matching condition, we understand that the air-hole diameter, d_a, has consequential dominance on the sensing performance as shown in Fig. 7(a) and (b) for both 6 and 8-fold PQF-RIBS. In both the sensors, the d_a value is kept as maximum as possible for the fabrication feasibility. When the d_a is optimized to 1 μm and further if it is increased, the electric field becomes more condensed in the core region and eventually reduces the surface excitation of the SPP which is essential for the sensing principle. Contrastingly, for $d_a > 1$ the n_{eff} of core-guided mode decreases and the electric field gets distributed in the cladding region. Therefore, the confinement loss increases, which, in turn, will avert the experimental execution. In general, during practical realization, if the confinement loss is increased, the SNR limits to identify the analyte. From this, it is clear that if the PQF-RIBS geometric parameters are varied for $\pm$ 10% from the optimized parameters, the proposed sensors' performance will not be hindered.

Further, we investigate the sensing channel thickness as shown in Fig. 7(c) and (d) for 6 and 8-fold, respectively. In view of easy experimental approach, maximum sensing channel thickness is expected for flexible analyte flow. From Fig. 7(c) and 7(d), it is clear that the propagation ls is unaffected with the increase of sensing channel thickness and the resonant wavelength variation to be identical. It is also interesting to note that the resonant wavelength is unchanged. Owing to the large analyte channel thickness, the proposed sensing systems are capable of allowing an easy analyte flow process.

To experimentally realize the proposed sensors, it is endorsed to implement the traditional stack and draw method [39]. Due to its diverse arrangements of air-holes, the sol-gel technique is also an alternate fabricating process. Usually, the sol-gel technique provides the well-arranged air-holes of microstructured optical fibers [40]. However, maintaining the uniform thickness of the metal layer on the outer surface of circular PQF-RIBS is challenging. Several metal-coating methods, such as radio frequency sputtering, thermal evaporation and wet-chemistry deposition which are used to coat the metal on the surface of sensing probes, result in surface roughness [41–43]. Chemical vapour deposition minimizes this surface roughness and improves the uniform coating on the circular sensing probes [44]. Further, the gold atomic layer deposition technique provides more uniform deposition on the circular fiber surface [45]. The sensing performance comparison of the proposed PQF-RIBS and reported sensors are listed in Table 2. Finally, by following the propagation loss measurement of the fibers, the proposed PQF-RIBS sensing performance could be explored.

Conclusion

In summary, a RI based biological and chemical sensing photonic quasicrystal fiber microbiosensors have been investigated by using finite element method. The sensing performance has been carried for the two different folds (6 and 8-folds) of photonic quasicrystal fiber sensors. Of the two folds, the 6-fold plasmonic sensor exhibits the spectral sensitivity of 28000 nm/RIU, with a resolution of 3.5×10^{-7}RIU, as calculated by the wavelength interrogation method. Besides, the modelled sensor indicates a profound amplitude sensitivity of 1095 RIU^{-1} and its corresponding resolution is 9.1×10^{-8} RIU for refractive index environment of 1.37 to 1.42. In order to quantify the performance of the sensor, we have also computed the figure of merit of the sensor and it turns out to be 491 for the 6-fold. It has been further inferred that the sensor performance appreciably increases when the folds of air-holes at

Table 2
Comparison of the proposed plasmonic sensors' performance with current sensors.

Ref.	Fiber structure	RI-range	Wave. Sens. (nm/RIU)	Resolution (Wave. Int.) (RIU)	Amp. Sens. (RIU-1)	Resolution (Amp. Int.) (RIU)
[29]	Spiral PCF	1.33–1.38	4600	3.62×10^{-5}	371.5	2.69×10^{-5}
[30]	SPR PCF	1.33–1.35	12600	1.583×10^{-5}	547.656	1.57×10^{-5}
[31]	Circular lattice PCF	1.34–1.37	9000	1.11×10^{-5}	318	–
[33]	SPR PCF	1.390–1.395	11000	9.09×10^{-5}	641	–
[35]	SPR PCF	1.33–1.37	4000	2.5×10^{-5}	478	2.1×10^{-5}
[46]	SPR PCF	1.46–1.48	10800	9.25×10^{-6}	514	2.7×10^{-5}
[47]	SPR PCF	1.36–1.39	6000	1.66×10^{-5}	442.11	–
[48]	SPR Circular PCF	1.35–1.37	8500	1.16×10^{-5}	335	–
[49]	SPR PCF	1.34–1.37	9000	1.11×10^{-5}	318	–
[50]	SPR PCF	1.33–1.41	18000	5.6×10^{-6}	2843	3.5×10^{-6}
[51]	LC PCF	1.33–1.34	3700	–	47.77	–
[52]	SPR PCF	1.33–1.39	30000	$3.33 \times 10 \text{textsuperscript} - 6$	1212	8.2×10^{-6}
[53]	SPP PCF	1.33–1.43	62000	1.61×10^{-6}	1415	–
Proposed work	6-fold PQF-RIBS	1.37–1.42	28000	3.5×10^{-7}	1095	9.1×10^{-8}
	8-fold PQF-RIBS	1.37–1.41	27000	9.8×10^{-7}	86	1.1×10^{-5}

the core region are increased. While for the 8-fold plasmonic sensor, the sensitivity turns a maximum of 27,000 nm/RIU for the refractive index environment of 1.39 to 1.40, it is 10,000 nm/RIU for the 6-fold plasmonic sensor. With the best response of the demonstrated PQF-RIBS over structural parameters, we envisage that the practical realization of the proposed sensors is quite direct. Hence, we are enormously hopeful that the proposed sensors would be highly suitable for the refractive-index based biological and chemical detections.

Acknowledgements

References

[1] Ng SS, Chan TO, To KW, Ngai J, Tung A, Ko FW, et al. Validation of Embletta portable diagnostic system for identifying patients with suspected obstructive sleep apnoea syndrome (OSAS). Respirology 2010;15(2):336–42. https://doi.org/10.1111/j.1440-1843.2009.01697.x.

[2] Dingli K, Coleman EL, Vennelle M, Finch SP, Wraith PK, Mackay TW, et al. Evaluation of a portable device for diagnosing the sleep apnoea/hypopnoea syndrome. Eur Respiratory J 2003;21(2):253–9.

[3] Gardeniers JG, van den Berg A. Lab-on-a-chip systems for biomedical and environmental monitoring. Anal Bioanal Chem 2004;378(7):1700–3.

[4] Gandhi MSA, Chu S, Senthilnathan K, Babu PR, Nakkeeran K, Li Q. Recent advances in plasmonic sensor-based fiber optic probes for biological applications. Appl Sci 2019;9(5):949.

[5] Goodrich TT, Lee HJ, Corn RM. Direct detection of genomic DNA by enzymatically amplified SPR imaging measurements of RNA microarrays. J Am Chem Soc 2004;126(13):4086–7.

[6] Fang Y. Label-free cell-based assays with optical biosensors in drug discovery. Assay Drug Develop Technol 2006;4(5):583–95.

[7] Fang S, Lee HJ, Wark AW, Corn RM. Attomole microarray detection of microRNAs by nanoparticle-amplified SPR imaging measurements of surface polyadenylation reactions. J Am Chem Soc 2006;128(43):14044–6.

[8] Liedberg B, Nylander C, Lunström I. Surface plasmon resonance for gas detection and biosensing. Sens Actuators 1983;4:299–304.

[9] Hasan M, Akter S, Rifat A, Rana S, Ali S. A highly sensitive gold-coated photonic crystal fiber biosensor based on surface plasmon resonance. Photonics. Multidisciplinary Digital Publishing Institute; 2017. p. 18. vol. 4.

[10] Azzam SI, Hameed MFO, Shehata REA, Heikal AM, Obayya SSA. Multichannel photonic crystal fiber surface plasmon resonance based sensor. Opt Quantum Electron 2016;48(2):142.

[11] Gupta BD. Surface plasmon resonance based fiber optic sensors; 2012.

[12] Dash JN, Jha R. Graphene-based birefringent photonic crystal fiber sensor using surface plasmon resonance. IEEE Photon Technol Lett 2014;26(11):1092–5. https://doi.org/10.1109/LPT.2014.2315233.

[13] Khalil AE, El-Saeed AH, Ibrahim MA, Hashish ME, Abdelmonem MR, Hameed MFO, et al. Highly sensitive photonic crystal fiber biosensor based on titanium nitride. Opt Quantum Electron 2018;50(3):158.

[14] Rifat AA, Mahdiraji GA, Sua YM, Ahmed R, Shee YG, Adikan FRM. Highly sensitive multi-core flat fiber surface plasmon resonance refractive index sensor. Opt Express 2016;24(3):2485–95. https://doi.org/10.1364/OE.24.002485.

[15] Luan N, Wang R, Lv W, Yao J. Surface plasmon resonance sensor based on D-shaped microstructured optical fiber with hollow core. Opt Express 2015;23(7):8576–82.

https://doi.org/10.1364/OE.23.008576.

[16] Kim S, Kee CS, Lee J. Novel optical properties of six-fold symmetric photonic quasicrystal fibers. Opt Express 2007;15(20):13221–6. https://doi.org/10.1364/OE.15.013221.

[17] Sun X, Hu DJJ. Air guiding with photonic quasi-crystal fiber. IEEE Photon Technol Lett 2010;22(9):607–9. https://doi.org/10.1109/LPT.2010.2043251.

[18] Gandhi MSA, Sivabalan S, Babu PR, Senthilnathan K. Designing a biosensor using a photonic quasi-crystal fiber. IEEE Sens J 2016;16(8):2425–30. https://doi.org/10.1109/JSEN.2016.2514850.

[19] Wang S, Sun X, Wang C, Peng G, Qi Y, Wang X. Liquid refractive index sensor based on a 2D 10-fold photonic quasicrystal. J Phys D 2017;50(36):365102https://doi.org/10.1088/1361-6463/aa7c56.

[20] Liu E, Tan W, Yan B, Xie J, Ge R, Liu J. Broadband ultra-flattened dispersion, ultra-low confinement loss and large effective mode area in an octagonal photonic quasi-crystal fiber. J Opt Soc Am A 2018;35(3):431–6. https://doi.org/10.1364/JOSAA.35.000431.

[21] Liu E, Liang S, Liu J. Double-cladding structure dependence of guiding characteristics in six-fold symmetric photonic quasi-crystal fiber. Superlattices Microstruct 2019;130:61–7. https://doi.org/10.1016/j.spmi.2019.03.011.

[22] Liu Q, Yan B, Liu J. U-shaped photonic quasi-crystal fiber sensor with high sensitivity based on surface plasmon resonance. Appl Phys Express 2019;12(5):052014https://doi.org/10.7567/1882-0786/ab13bc.

[23] Chu S, Nakkeeran K, Abobaker AM, Aphale SS, Babu PR, Senthilnathan K. Design and analysis of surface-plasmon-resonance-based photonic quasi-crystal fiber biosensor for high-refractive-index liquid analytes. IEEE J Sel Top Quantum Electron 2019;25(2):1–9. https://doi.org/10.1109/JSTQE.2018.2873481.

[24] Wang JN, Tang JL. Photonic crystal fiber mach-zehnder interferometer for refractive index sensing. Sensors 2012;12(3):2983–95. https://doi.org/10.3390/s120302983.

[25] Lu Y, Hao CJ, Wu BQ, Musideke M, Duan LC, Wen WQ, et al. Surface plasmon resonance sensor based on polymer photonic crystal fibers with metal nanolayers. Sensors 2013;13(1):956–65. https://doi.org/10.3390/s130100956.

[26] Rifat AA, Ahmed R, Yetisen AK, Butt H, Sabouri A, Mahdiraji GA, et al. Photonic crystal fiber based plasmonic sensors. Sens Actuators B: Chem 2017;243:311–25. https://doi.org/10.1016/j.snb.2016.11.113.

[27] Liu M, Yang X, Shum P, Yuan H. High-sensitivity birefringent and single-layer coating photonic crystal fiber biosensor based on surface plasmon resonance. Appl Opt 2018;57(8):1883–6. https://doi.org/10.1364/AO.57.001883.

[28] Rifat AA, Haider F, Ahmed R, Mahdiraji GA, Adikan FRM, Miroshnichenko AE. Highly sensitive selectively coated photonic crystal fiber-based plasmonic sensor. Opt Lett 2018;43(4):891–4. https://doi.org/10.1364/OL.43.000891.

[29] Hasan MR, Akter S, Rifat AA, Rana S, Ahmed K, Ahmed R, et al. Spiral photonic crystal fiber-based dual-polarized surface plasmon resonance biosensor. IEEE Sens J 2018;18(1):133–40. https://doi.org/10.1109/JSEN.2017.2769720.

[30] Hameed MFO, Alrayk YKA, Obayya SSA. Self-calibration highly sensitive photonic crystal fiber biosensor. IEEE Photon J 2016;8(3):1–12. https://doi.org/10.1109/JPHOT.2016.2563319.

[31] Chakma S, Khalek MA, Paul BK, Ahmed K, Hasan MR, Bahar AN. Gold-coated photonic crystal fiber biosensor based on surface plasmon resonance: design and analysis. Sens Bio-Sens Res 2018;18:7–12. https://doi.org/10.1016/j.sbsr.2018.02.003.

[32] Li X, Li S, Yan X, Sun D, Liu Z, Cheng T. High sensitivity photonic crystal fiber refractive index sensor with gold coated externally based on surface plasmon resonance. Micromachines 2018;9(12):640. https://doi.org/10.3390/mi9120640.

[33] Zhou X, Cheng T, Li S, Suzuki T, Ohishi Y. Practical sensing approach based on surface plasmon resonance in a photonic crystal fiber. OSA Continuum 2018;1(4):1332–40. https://doi.org/10.1364/OSAC.1.001332.

[34] Rifat AA, Hasan MR, Ahmed R, Butt H. Photonic crystal fiber-based plasmonic biosensor with external sensing approach (erratum). J Nanophoton 2018;12(1):019901https://doi.org/10.1117/1.JNP.12.019901.

[35] Gandhi MA, Babu PR, Senthilnathan K, Li Q. High sensitivity photonic crystal fiber-based refractive index microbiosensor. Opt Fiber Technol 2018;46:88–94. https://

doi.org/10.1016/j.yofte.2018.09.016.

[36] Sellmeier W. Zur Erkarung der abnormen Farbenfolge im Spectrum einiger. Substanzen. Ann Phys Chem 1871;219:272–82.

[37] Vial A, Grimault AS, Macías D, Barchiesi D, de la Chapelle ML. Improved analytical fit of gold dispersion: application to the modeling of extinction spectra with a finite-difference time-domain method. Phys Rev B 2005;71(8):085416https://doi.org/10.1103/PhysRevB.71.085416.

[38] Shaban M, Ahmed AM, Abdel-Rahman E, Hamdy H. Tunability and sensing properties of plasmonic/1D photonic crystal. Scientific Rep 2017;7..

[39] Russell P. Photonic crystal fibers. Science 2003;299(5605):358–62. https://doi.org/10.1126/science.1079280.

[40] Bise RT, Trevor D. Solgel-derived microstructured fibers: fabrication and characterization. Optical fiber communication conference and exposition and the national fiber optic engineers conference. Optical Society of America; 2005. p. 6.

[41] Armelao L, Barreca D, Bottaro G, Bruno G, Gasparotto A, Losurdo M, et al. RF-sputtering of gold on silica surfaces: Evolution from clusters to continuous films. Mater Sci Eng: C 2005;25(5):599–603. https://doi.org/10.1016/j.mSection 2005.06.007.

[42] Barnes MC, Kim DY, Ahn HS, Lee CO, Hwang NM. Deposition mechanism of gold by thermal evaporation: approach by charged cluster model. J Crystal Growth 2000;213(1):83–92. https://doi.org/10.1016/S0022-0248(00)00359-6.

[43] Sioss JA, Keating CD. Batch preparation of linear Au and Ag nanoparticle chains via wet chemistry. Nano Lett 2005;5(9):1779–83. https://doi.org/10.1021/nl051370u.

[44] Sazio PJA, Amezcua-Correa A, Finlayson CE, Hayes JR, Scheidemantel TJ, Baril NF, et al. Microstructured optical fibers as high-pressure microfluidic reactors. Science 2006;311(5767):1583–6. https://doi.org/10.1126/science.1124281.

[45] Griffiths MBE, Pallister PJ, Mandia DJ, Barry ST. Atomic layer deposition of gold

metal. Chem Mater 2016;28(1):44–6. https://doi.org/10.1021/acs.chemmater.5b04562.

[46] Hasan MR, Akter S, Rahman MS, Ahmed K. Design of a surface plasmon resonance refractive index sensor with high sensitivity. Opt Eng 2017;56(8). https://doi.org/10.1117/1.OE.56.8.087101.

[47] Hossen MN, Ferdous M, Khalek MA, Chakma S, Paul BK, Ahmed K. Design and analysis of biosensor based on surface plasmon resonance. Sens Bio-Sens Res 2018;21:1–6. https://doi.org/10.1016/j.sbsr.2018.08.003.

[48] Asaduzzaman S, Ahmed K. Investigation of ultra-low loss surface plasmon resonance-based PCF for biosensing application. Results Phys 2018;11:358–61. https://doi.org/10.1016/j.rinp.2018.09.026.

[49] Khalek MA, Chakma S, Paul BK, Ahmed K. Dataset of surface plasmon resonance based on photonic crystal fiber for chemical sensing applications. Data Brief 2018;19:76–81. https://doi.org/10.1016/j.dib.2018.05.026.

[50] Haider F, Aoni RA, Ahmed R, Miroshnichenko AE. Highly amplitude-sensitive photonic-crystal-fiber-based plasmonic sensor. J Opt Soc Am B 2018;35(11):2816–21. https://doi.org/10.1364/JOSAB.35.002816.

[51] Azab MY, Hameed MFO, Obayya SSA. Multi-functional optical sensor based on plasmonic photonic liquid crystal fibers. Opt Quantum Electron 2017;49(2):49. https://doi.org/10.1007/s11082-016-0849-7.

[52] Haider F, Aoni RA, Ahmed R, Islam MS, Miroshnichenko AE. Propagation controlled photonic crystal fiber-based plasmonic sensor via scaled-down approach. IEEE Sens J 2019;19(3):962–9. https://doi.org/10.1109/JSEN.2018.2880161.

[53] Islam MS, Sultana J, Rifat AA, Ahmed R, Dinovitser A, Ng BWH, et al. Dual-polarized highly sensitive plasmonic sensor in the visible to near-IR spectrum. Opt Express 2018;26(23):30347–61. https://doi.org/10.1364/OE.26.030347.